Article

Neural Network Reflectance Prediction Model for Both Open Ocean and Coastal Waters

Lipi Mukherjee [1], Peng-Wang Zhai [1,*], Meng Gao [2], Yongxiang Hu [3], Bryan A. Franz [4] and P. Jeremy Werdell [4]

[1] Joint Center for Earth Systems Technology, Department of Physics, University of Maryland, Baltimore County, 1000 Hilltop Circle Baltimore, Baltimore, MD 21250, USA; lipimuk1@umbc.edu
[2] SSAI, NASA Goddard Space Flight Center, Code 616, Greenbelt, MD 20771, USA; meng.gao@nasa.gov
[3] MS 475 NASA Langley Research Center, Hampton, VA 23681-2199, USA; yongxiang.hu-1@nasa.gov
[4] NASA Goddard Space Flight Center, Code 616, Greenbelt, MD 20771, USA; bryan.a.franz@nasa.gov (B.A.F.); jeremy.werdell@nasa.gov (P.J.W.)
* Correspondence: pwzhai@umbc.edu

Abstract: Remote sensing of global ocean color is a valuable tool for understanding the ecology and biogeochemistry of the worlds oceans, and provides critical input to our knowledge of the global carbon cycle and the impacts of climate change. Ocean polarized reflectance contains information about the constituents of the upper ocean euphotic zone, such as colored dissolved organic matter (CDOM), sediments, phytoplankton, and pollutants. In order to retrieve the information on these constituents, remote sensing algorithms typically rely on radiative transfer models to interpret water color or remote-sensing reflectance; however, this can be resource-prohibitive for operational use due to the extensive CPU time involved in radiative transfer solutions. In this work, we report a fast model based on machine learning techniques, called Neural Network Reflectance Prediction Model (NNRPM), which can be used to predict ocean bidirectional polarized reflectance given inherent optical properties of ocean waters. This supervised model is trained using a large volume of data derived from radiative transfer simulations for coupled atmosphere and ocean systems using the successive order of scattering technique (SOS-CAOS). The performance of the model is validated against another large independent test dataset generated from SOS-CAOS. The model is able to predict both polarized and unpolarized reflectances with an absolute error (AE) less than 0.004 for 99% of test cases. We have also shown that the degree of linear polarization (DoLP) for unpolarized incident light can be predicted with an AE less than 0.002 for 99% of test cases. In general, the simulation time of SOS-CAOS depends on optical depth, and required accuracy. When comparing the average speeds of the NNRPM against the SOS-CAOS model for the same parameters, we see that the NNRPM is able to predict the Ocean BRDF 6000 times faster than SOS-CAOS. Both ultraviolet and visible wavelengths are included in the model to help differentiate between dissolved organic material and chlorophyll in the study of the open ocean and the coastal zone. The incorporation of this model into the retrieval algorithm will make the retrieval process more efficient, and thus applicable for operational use with global satellite observations.

Keywords: radiative transfer; retrieval; reflectance model; polarization; ocean optics; neural network

1. Introduction

The study of global ocean color measurements can help in understanding the ocean ecology and biogeochemistry which can subsequently help better understand the carbon cycle and its impact on climate change. Ocean polarized reflectances obtained from satellite sensors contain a lot of information

about the constituents like colored dissolved organic matter (CDOM), sediments, phytoplankton, and pollutants in water. In order to retrieve this information, ocean color remote sensing algorithms retrieve remote sensing reflectances (R_{rs}, sr^{-1}) from the sensor measurement at the top of the atmosphere (TOA) through atmospheric correction, which removes the contribution of atmospheric and ocean surface effects from the total signal [1–3].

Once remote sensing reflectance is obtained, empirical and model based approaches [4–11] are developed to retrieve the inherent optical properties (IOPs). One such empirical approach is the band ratio method which statistically relates R_{rs} at two or more wavelengths to a particular water constituent. The algorithm quantifies water constituents as a function of blue and green light emanating from the ocean surface [4,12]. Another empirical approach is based on a line-height color index that is the difference between R_{rs} in the green band and a reference formed linearly between remote sensing reflectance in the blue and red band [5]. The second approach performs better in areas with adjacency effects, such as sun glint or cloud edges. Both empirical approaches are successful for open ocean where the phytoplankton and detrital are the main constituents of water, co-varying with each other [13]. However, they often perform less successfully for coastal ocean where the optical constituents like CDOM and suspended sediments do not co-vary with water primary productivity.

The model based approach uses bio-optical models, most of which are empirically derived, to describe the relationship between in-water constituents and inherent optical properties (IOP's). Radiative transfer models are then used to relate the reflectance spectra to the desired in-water constituents. Semi-analytical models fall within the category of model based algorithms. There are several semi-analytical models developed with different assumptions and limitations [6]. They essentially follow different empirical relationships of spectral shape functions or eigenvectors of the constituent absorption and scattering components. Thereafter, the optimized magnitudes or eigenvalues representing the relative contributions of each constituent is obtained by minimizing the difference between modelled and measured reflectance values (R_{rs}) [14,15]. Those algorithms cannot predict the polarization of ocean reflectance and are not valid in the ultraviolet wavelength range.

Both empirical and model based methods depend on a reliable atmospheric correction algorithm. However, due to the presence of absorbing aerosols and complex optical properties of coastal waters, it is difficult to achieve successful atmospheric correction over coastal waters or when absorbing aerosols are involved [16,17]. To overcome the limitations of atmospheric correction in coastal and inland waters involving absorbing aerosols, the community proposes to use multi-angle multi-wavelength, polarized measurements to characterize aerosol and hydrosol properties. The polarized signal is measured by several multiangular polarimeters like POLDER [18], the Research Scanning Polarimeter (RSP) [19], the Airborne Multiangle SpectroPolarimetric Imager (AirMSPI) [20], the Spectropolarimeter for Planetary EXploration (SPEX) [21] and the HyperAngular Rainbow Polarimeter (HARP) [22]. it is worth noting that NASA's Plankton, Aerosol, Cloud, ocean Ecosystem (PACE) mission plans to carry SPEXone and HARP2 as well as the Ocean Color Instrument (OCI), which will acquire a plethora of unprecedented co-located datasets of polarimeter and ocean color measurements [23].

In order to take advantage of the polarimeter measurements, joint retrieval algorithms are developed to simultaneously retrieve information of aerosols and hydrosols [24–26]. The bio-optical models used by the aforementioned joint retrieval algorithms are for open ocean and thus are ill-suited for coastal waters. Recently, the Multi-Angle Polarimetric Ocean coLor (MAPOL) retrieval algorithm [27] has been designed specifically for the optically complex coastal waters and aerosols for improved atmospheric correction. MAPOL has been demonstrated over both open ocean and coastal waters, which shows promising applications in achieving atmospheric correction over complex scenes [27]. The joint retrieval algorithms, including MAPOL, need to call radiative transfer models iteratively in order to minimize the difference between measurements and model prediction, which is computationally expensive and difficult to achieve operational production. It is critical to develop

a fast ocean reflectance model that can be used in the joint retrieval algorithms to achieve operational retrieval of aerosol and ocean color information.

Recently, Fan et al. [28] have created a neural network to model the ocean body reflection matrix based on 3 parameters. In this work, we present an ocean reflectance model based on machine learning techniques, hereafter referred to as Neural Network Reflectance Prediction Model (NNRPM), which can be used to replace the radiative transfer simulation of ocean waters and expedite the retrieval algorithm significantly. This model incorporates additional parameters that would enable it to be better used for coastal waters. Moreover, it can also be used in semi-analytical models that retrieve IOPs from water leaving radiance or equivalent remote sensing reflectance. The basic advantages of neural networks are exploited, namely their accuracy performance properties, their robustness to noise, and their rapidity of execution.

This paper is organized as follows: Section 2 describes the methodology and definitions used in this work; Section 3 shows the result of this study; Section 4 summarizes the conclusion reached in this study.

2. Methods

Our goal is to build a polarized reflectance model for ocean waters. The ocean water model is the same as the one used in the MAPOL algorithm [27,29]. In order to model the optical properties of coastal waters the ocean water is assumed to consist of four components: pure sea water, phytoplankton particles, non-algae particles (NAP), and CDOM. The absorption coefficient $a_w(\lambda)$ and scattering coefficient $b_w(\lambda)$ for pure sea water are from the experimental data [30–32]. The backscattering fraction for water is 0.5 [33]. We denote the absorption coefficient for phytoplankton as $a_{ph}(\lambda)$, the total absorption coefficient for both CDOM and NAP as $a_{dg}(\lambda)$, the total backscattering coefficient and total backscattering fraction for both phytoplankton and NAP as $b_{bp}(\lambda)$ and $B_p(\lambda)$. The scattering coefficient of CDOM is assumed to be negligible. The bio-optical model can be written as [29]:

$$
\begin{aligned}
a_{ph}(\lambda) &= A_{ph}(\lambda)[\text{Chla}]^{E_{ph}(\lambda)}, \\
a_{dg}(\lambda) &= a_{dg}(440)\exp[-S_{dg}(\lambda - 440)], \\
b_{bp}(\lambda) &= b_{bp}(660)(\lambda/660)^{-S_{bp}}, \\
B_p(\lambda) &= B_p(660)(\lambda/660)^{-S_{Bp}},
\end{aligned}
\tag{1}
$$

where wavelength (λ) is in nm; $a_{ph}(\lambda)$ is determined by [Chla], A_{ph}, and E_{ph}; [Chla] is in units of mg/m^3. Values of the coefficients A_{ph}, and E_{ph} are obtained from Bricaud et al. [34]. S_{dg} is the exponential spectral slope for $a_{dg}(\lambda)$; S_{bp} and S_{Bp} are the polynomial spectral slopes for $b_{bp}(\lambda)$ and $B_p(\lambda)$ respectively. The total absorption coefficient is $a(\lambda) = a_w(\lambda) + a_{ph}(\lambda) + a_{dg}(\lambda)$, and the total backscattering coefficient is $b_b(\lambda) = 0.5b_w(\lambda) + b_{bp}(\lambda)$. The inherent optical properties (IOPs), $a_{ph}(\lambda)$, $a_{dg}(\lambda)$, $b_{bp}(\lambda)$, $a_w(\lambda)$, and $b_w(\lambda)$ are used to describe the ocean color spectrum in ocean bio-optical models [11,15,35]. Generalised IOP (GIOP) model is also used in the earth science community [35,36].

The Fournier-Forand (FF) [37] phase function is used to represent the phase functions of both phytoplankton and NAP, which is in agreement with various in-situ volume scattering function (VSF) measurements [38]. The scattering coefficient of the phytoplankton and NAP particles can be derived from $b_p = b_{bp}/B_p$. The determination of the FF phase function [39] is done by backscattering fraction B_{bp} [39]. The total phase function for the coastal water system is obtained by mixing the FF phase function with the pure seawater phase function weighted by the scattering coefficients of the constituents. The normalized Mueller matrix is from measurements from average ocean waters [40–42]. The ocean water is assumed to be vertically homogeneous with a depth of 200 m. The minimum and maximum values of the parameters [29] considered are given in Table 1.

Table 1. Minimum and maximum values of parameters in the bio-optical models mentioned in Equation (1).

Parameter	Chla	$a_{dg}(440)$	$b_{bp}(660)$	$B_p(660)$	S_{dg}	S_{bp}	S_{Bp}
Unit	mg/m^3	m^{-1}	m^{-1}		nm^{-1}	nm^{-1}	nm^{-1}
Min	~0.0	~0.0	~0.0	~0.0	0.01	0.0	−0.2
Max	30.0	2.5	0.1	0.05	0.02	0.5	0.2

Here, we are focusing on the coastal waters so that the particle size is primarily large. In addition to the aforementioned parameters, viewing zenith angles range from 0 to 87.5° with an interval of 2.5°. The viewing azimuth angles are from 0 to 180° with an interval of 5°. The incident zenith angles are taken from 0 to 85°. The wavelengths used are 385, 410, 440, 470, 555, 670, 760, 863.5, and 870 nm. The aforementioned wavelengths include the ultraviolet, visible and near infrared (VNIR) part of the electromagnetic spectrum. The wavelengths 410, 470, 555, 670, and 863.5 nm are used as part of research scanning polarimeter (RSP) and the rest are adopted based on other existing and new ocean color sensors. The above mentioned bio-optical parameters, wavelengths, incident zenith angles (θ_i), viewing zenith and azimuth angles were provided as inputs to the radiative transfer code based on successive order of scattering for coupled atmosphere and ocean systems (SOS-CAOS) [43,44]. There is no atmosphere in our radiative transfer simulation as we are focused on the ocean reflectance model. Glint from the ocean surface can be predicted analytically, which is excluded in this simulation. The output of the radiative transfer simulations were considered as the true or desired value while training the neural network.

The objective of the neural network is to predict the non-dimensional effective Mueller matrix [45], M as a function of the wavelength λ, viewing zenith angle θ_v, viewing azimuth angle ϕ_v, incident zenith angle θ_i, and incident azimuth angle ϕ_i:

$$M(\lambda, \theta_v, \theta_i, \phi_v - \phi_i) = \begin{bmatrix} M_{11} & M_{12} & M_{13} & M_{14} \\ M_{21} & M_{22} & M_{23} & M_{24} \\ M_{31} & M_{32} & M_{33} & M_{34} \\ M_{41} & M_{42} & M_{43} & M_{44} \end{bmatrix}. \tag{2}$$

We denote the radiance column vector as $L = (I, Q, U, V)^T$, where (I, Q, U, V) are the Stokes parameters representing the polarization state of a light beam and the superscript T stands for transpose.

Once M is obtained, the upwelling radiance vector $L(\theta_v, \phi_v)$ can be calculated from incident downwelling radiance vector $L(\theta_i, \phi_i)$. For an arbitrarily polarized incident light, the reflected radiance can be calculated from the following relation:

$$L(\theta_v, \phi_v) = \frac{1}{\pi} \int M(\theta_v, \theta_i, \phi_v - \phi_i) L(\theta_i, \phi_i) cos\theta_i dcos\theta_i d\phi_i, \tag{3}$$

where we have implicitly assumed the wavelength dependency of both M and L. Hereafter, we neglect the fourth column and row of M, due to their small contribution for oceanic environment [46]. The 3×3 Muller matrix M can be obtained by considering the following incident polarizations: (I_1, Q_1, U_1) as complete unpolarization (1,0,0), (I_2, Q_2, U_2) as horizontal polarization (1,1,0) and (I_3, Q_3, U_3) as 45° polarization (1,0,1) to get:

$$M = \frac{\pi}{F_0 cos\theta_i} \begin{bmatrix} I_{w1} & I_{w2} - I_{w1} & I_{w3} - I_{w1} \\ Q_{w1} & Q_{w2} - Q_{w1} & Q_{w3} - Q_{w1} \\ U_{w1} & U_{w2} - U_{w1} & U_{w3} - U_{w1} \end{bmatrix}, \tag{4}$$

where (I_{w1}, Q_{w1}, U_{w1}), (I_{w2}, Q_{w2}, U_{w2}), (I_{w3}, Q_{w3}, U_{w3}) represents remote sensing reflectance just above the ocean water surface corresponding to the three polarized incident beams. F_0 is the incident irradiance. The elements of the matrix in Equation (4), are obtained by solving SOS-CAOS [43,44]. As part of the neural network training, all the elements (except M_{11}) of the matrix in Equation (4) are normalized by M_{11}.

We have created a supervised, model based, batch learning, neural network algorithm with the architecture of a multilayer perceptron (MLP) using MATLAB's Neural Network package [47]. An MLP is a feedforward and backpropagated artificial neural network [48]. This neural network approximates the function relating the various inputs of the network to the output [49] and would be used to predict ocean bidirectional reflectance distribution function in this work [50]. The network was trained with 10 inputs (Chla, a_{dg}, b_{bp}, B_p, S_{Bp}, S_{bp}, S_{dg}, θ_i, θ_v and ϕ_v) and the output reflectance for every wavelength being studied.

Figure 1 shows the structure of the neural network used in this work. We arrived at the above architecture by using the general guidelines in [51] as the base and then modifying it as per the requirements of our dataset. The input layer has 10 inputs x_1 to x_{10}. The hidden layer consists of 4 layers each having 40 nodes. The output layer has one node. Each node has a summation operator and an activation function within it except the input nodes. The output of every node in a layer is multiplied by a weight and summed with the output of other weighted nodes in that layer and a bias to be fed as input to the activation function. The output of the activation function becomes the input of a node in the following layer. we have used tangent sigmoid as our activation function:

$$f = \text{tansig}(x) = \frac{2}{(1 + \exp(-2 * x))} - 1, \tag{5}$$

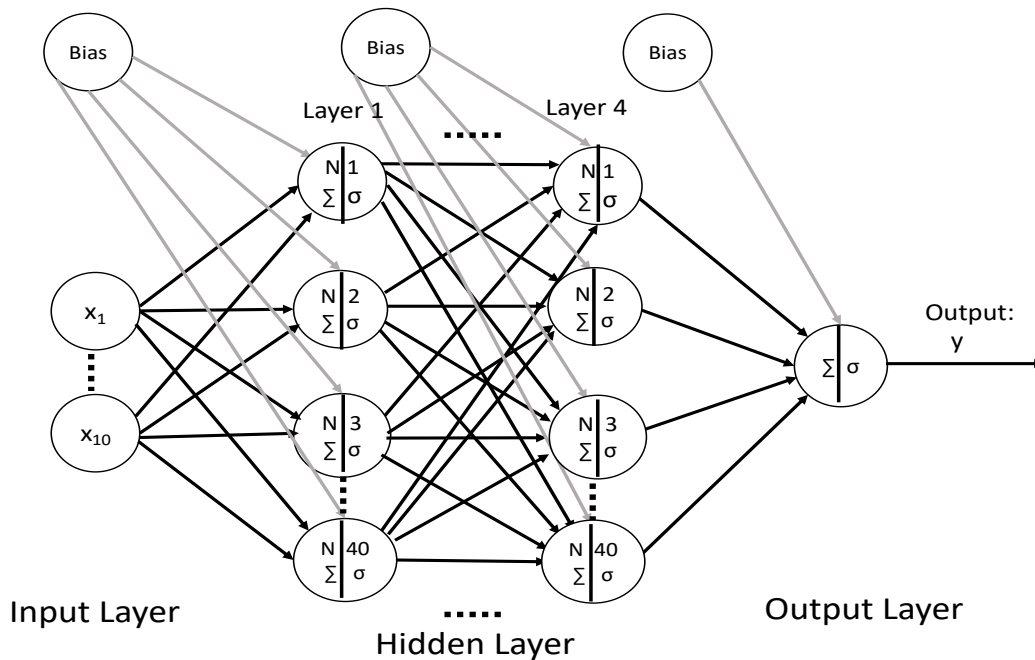where x denotes the sum of weighted nodes of the layer and the bias.

Figure 1. Structure of the neural network.

For each training instance this neural network algorithm first makes a prediction on the forward pass, measures the error, then goes through each layer in reverse to measure the error contribution from each previous connection (on the reverse pass), and finally tweaks each of the connection weights to reduce the error as part of Levenberg-Marquardt optimization algorithm [52]. So, essentially, we start off with random weight values and then improve it gradually one step at a time such that each step

reduces the error until the algorithm converges to a minimum. The Levenberg-Marquardt optimization algorithm can be represented as:

$$w_{k+1} = w_k - \left[J^T J + \mu I \right]^{-1} J^T e, \tag{6}$$

where w_k is the weight/bias of previous iteration and w_{k+1} is the weight/bias of next iteration. J is the Jacobian matrix and J^T is its transpose. J contains first derivatives of the network errors with respect to the weights and biases, and e is a vector of network errors. I is the identity matrix. The parameter μ determines direction as well as the length of the particular iteration step. It is a value that speeds up or slows down how quickly an algorithm learns. Technically, it determines the size of step an algorithm takes when moving towards a global minimum. Levenberg-Marquardt algorithm combines the Gauss-Newton and gradient descent optimizer methods. For larger values of μ, this algorithm will use gradient descent as the primary optimizer and for very small values of μ, Gauss-Newton would act as the primary optimizer. Here we have used $\mu = 10^{-4}$.

After each iteration of training, the performance of neural network was monitored on the test dataset by calculating the mean square error. In order to avoid over-fitting, the training was stopped when the mean square error continued to increase for 6 consecutive iterations on the test dataset [51]. The model equation can be represented as:

$$y = b_{5[1]} + \Sigma_{k=1}^{N_h} w_{5[1,k]}.f\langle b_{4[k]} + \Sigma_{k=1}^{N_h} w_{4[k,k]}.f\{b_{3[k]} + \Sigma_{k=1}^{N_h} w_{3[k,k]}.f[b_{2[k]} + \Sigma_{k=1}^{N_h} w_{2[k,k]}.f(b_{1[k]} + \Sigma_{l=1}^{N_i} w_{1[k,l]}.x_l)]\}\rangle, \tag{7}$$

where y is the output reflectance, predicted by the network. N_i is the number of input parameters, N_h is number of neurons in each hidden layer, $w_{1[k,l]}, w_{2[k,k]}, w_{3[k,k]}, w_{4[k,k]}$, and $w_{5[1,k]}$ are the weights of the four hidden layers and the output layer respectively, and $b_{1[k]}, b_{2[k]}, b_{3[k]}, b_{4[k]}$, and $b_{5[1]}$ are the biases of the four hidden layers and the output layer respectively. f is the tangent sigmoid activation function given in Equation (5). Figure 2 shows the high level flow diagram of the neural network.
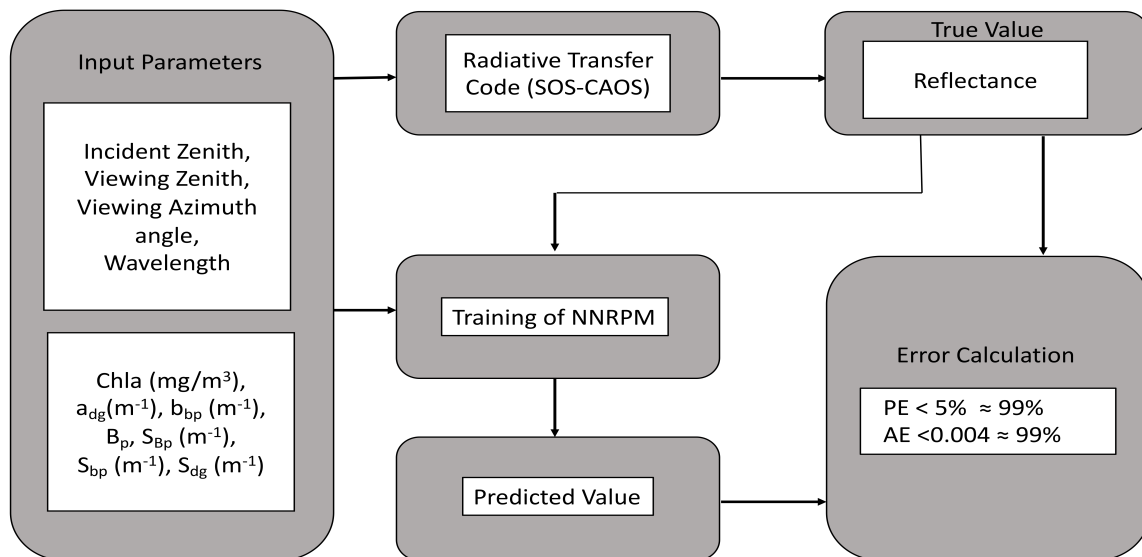

Figure 2. High level flow diagram for NNRPM.

Feature sequences for the various input parameters were generated using a quasi-random number sequence, the Halton sequence [53]. First introduced by Halton [54], it is constructed using a deterministic method and is of low discrepancy. Training and test datasets corresponding to the above sequences were generated by SOS-CAOS [43,44]. The neural network was trained and validated using the training and test datasets.

The error measurement for the element M_{11} is computed using the relation below:

$$\text{Percentage Error (PE)} = 100 \times \frac{|\text{True Value} - \text{Predicted Value}|}{\text{True Value}}. \tag{8}$$

In order to avoid the numerical difficulty of dividing by zero, the error measurement for all other normalized elements (M_{ij}/M_{11}) is computed using the relation below:

$$\text{Absolute Error (AE)} = |\text{True Value} - \text{Predicted Value}|. \tag{9}$$

The above errors are used to calculate the empirical cumulative distribution function, which gives the probability of the number of samples within a certain (error) value, which is used to illustrate the performance of the neural network. If $\{X_1, ..., X_n\}$ is an independently and identically distributed sample from an unknown distribution function, $F(x) = \mathbb{P}(X \leq x)$, then the empirical cumulative distribution function ($\hat{F}_n(x) \Rightarrow \text{ECDF}$) is defined as [55]:

$$\text{ECDF} = \frac{1}{n} \sum_{i=1}^{n} 1\{X_i \leq x\}, \tag{10}$$

where,

$$1\{X_i \leq x\} = \begin{cases} 1, & \text{if } X_i \leq x \\ 0, & \text{otherwise.} \end{cases} \tag{11}$$

Another metric used here to evaluate the performance of NNRPM is the Pearson correlation coefficient (R) [56]:

$$R = \frac{\sum_{i=1}^{n} (x_i - \bar{x})(y_i - \bar{y})}{\sqrt{\sum_{i=1}^{n} (x_i - \bar{x})^2} \sqrt{\sum_{i=1}^{n} (y_i - \bar{y})^2}}, \tag{12}$$

where n is the sample size, x_i and y_i are sample points, $\bar{x}$ and $\bar{y}$ are sample means of two variables x and y respectively.

3. Results

In Figure 3, we present a plot between error percentage and Halton sequences. Here, error percentage represents the percentage of test cases with absolute error greater than 0.004. At 8 K Halton sequences, the error percentage reached its minimum value and then varies little after that. This established the following relationship with error percentage and training Halton combinations (N):

$$\text{Error\%} \propto \frac{1}{N}. \tag{13}$$
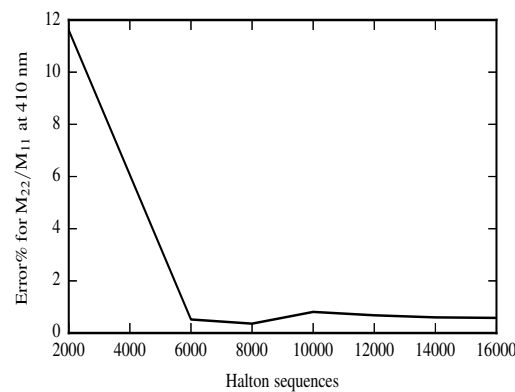
Figure 3. Error% versus Halton sequences for reduced M_{22}/M_{11} element at 410 nm.

In Figure 4, we have shown the performance of the neural network NNRPM by the linear regression plot between the true value calculated by SOS-CAOS and the predicted value predicted by NNRPM for elements M_{22}/M_{11} and M_{32}/M_{11} at wavelength 555 nm, for 1000 Halton sequence independently generated for validation.


(**a**)   (**b**)
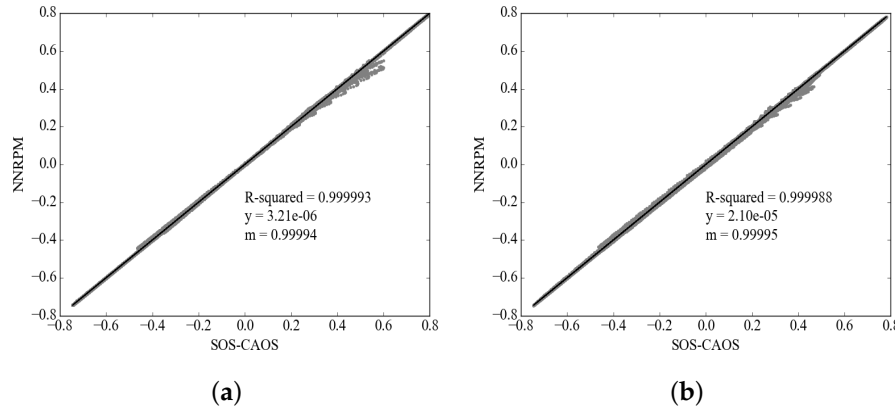
Figure 4. Linear regression between the true reflectance values generated by SOS-CAOS and those predicted by NNRPM for elements (**a**) M_{22}/M_{11} and (**b**) M_{32}/M_{11} at 555 nm for 1000 Halton sequences.

Figures 5 and 6 show the polar plots for the true value (SOS-CAOS), predicted value (NNRPM), and percentage error for the first element of the first column (M_{11}) for two different sets of input parameters for wavelengths 385 and 555 nm. Figures 7 and 8 show the polar plots for the true value (SOS-CAOS), predicted value (NNRPM), and absolute error for the reduced first element of the second column (M_{12}/M_{11}) for the same cases as shown in Figures 5 and 6. For each polar plot, the zenith point is at the center, and the viewing zenith angle of 67.5° is at the rim of the polar plot. The viewing azimuthal angles are shown around the plots.
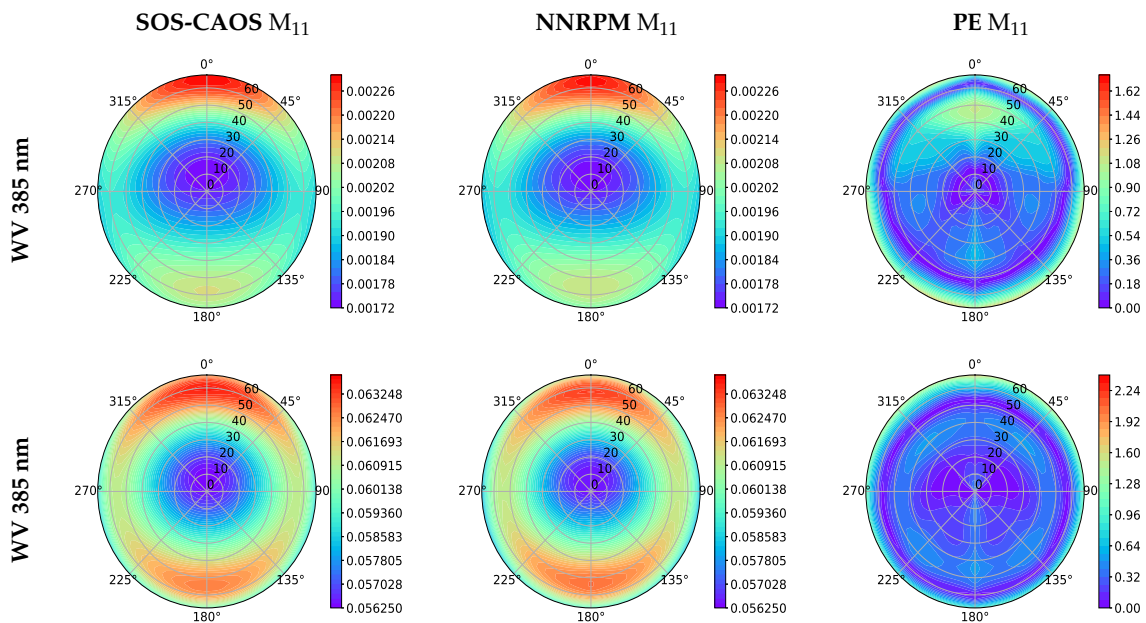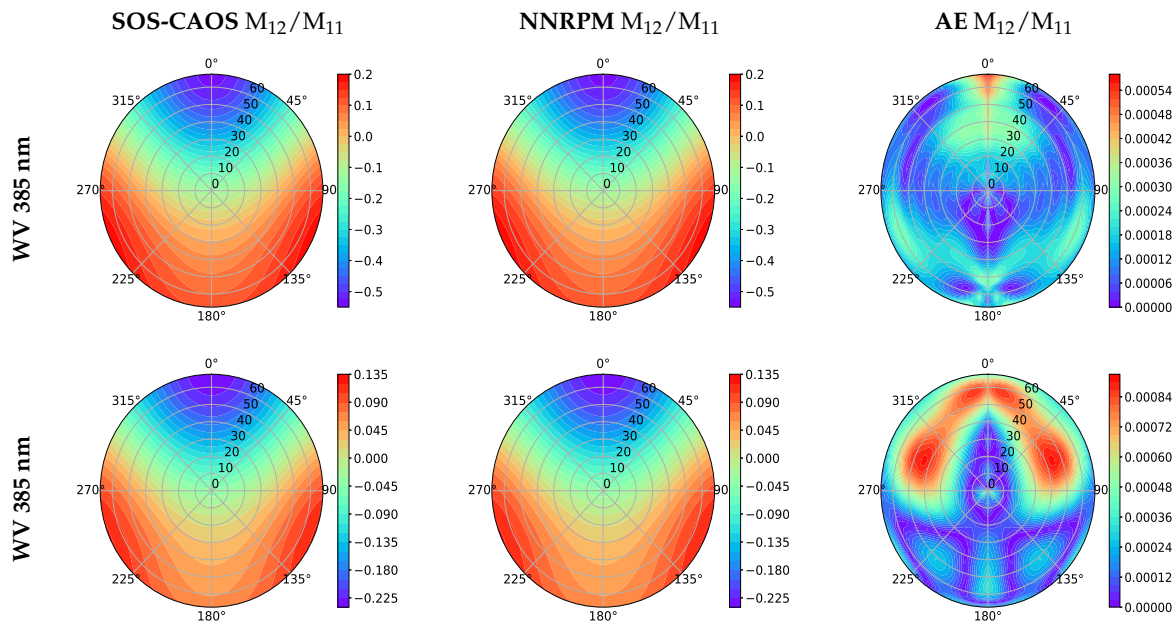

Figure 5. Polar plots of SOS-CAOS, NNRPM and PE for M_{11} at wavelength 385 nm. Input parameters for Top Row: $\theta_i = 55.91°$, Chla = 20.43 mg/m^3, $a_{dg}(440) = 7.36$ m^{-1}, $b_{bp} = 0.097$ m^{-1}, $B_P = 0.015$, $S_{Bp} = -0.157$ nm^{-1}, $S_{bp} = 0.258$ nm^{-1}, $S_{dg} = 0.019$ nm^{-1}. Input parameters for Bottom Row: $\theta_i = 43.02°$, Chla = 24.77 mg/m^3, $a_{dg}(440) = 0.004$ m^{-1}, $b_{bp} = 0.099$ m^{-1}, $B_P = 0.046$, $S_{Bp} = -0.106$ nm^{-1}, $S_{bp} = 0.023$ nm^{-1}, $S_{dg} = 0.014$ nm^{-1}.
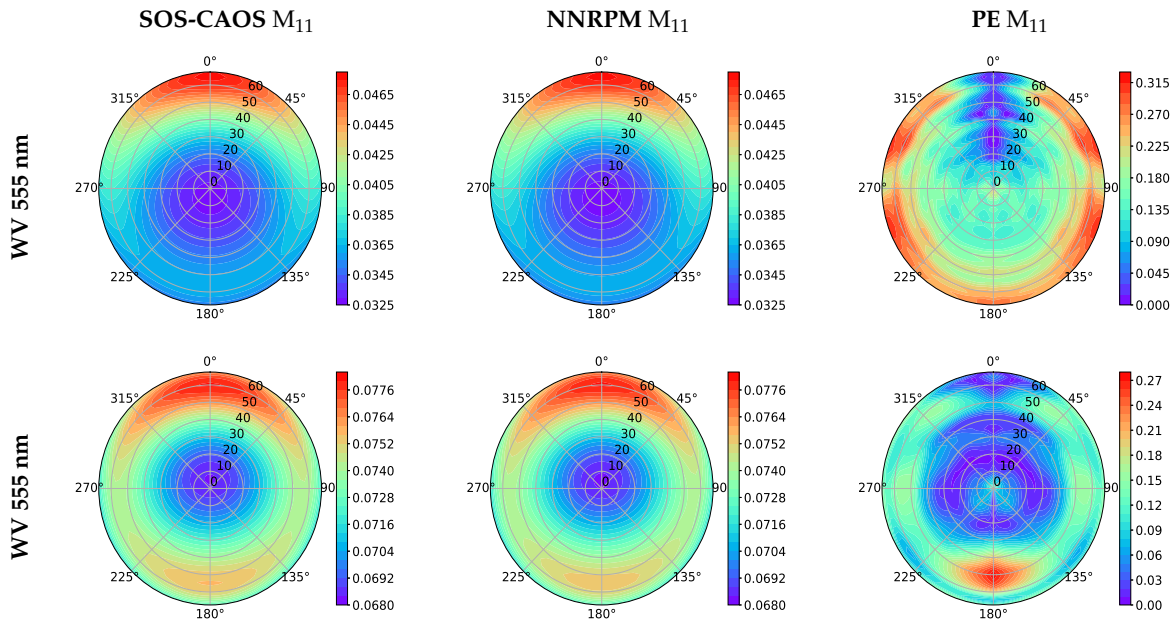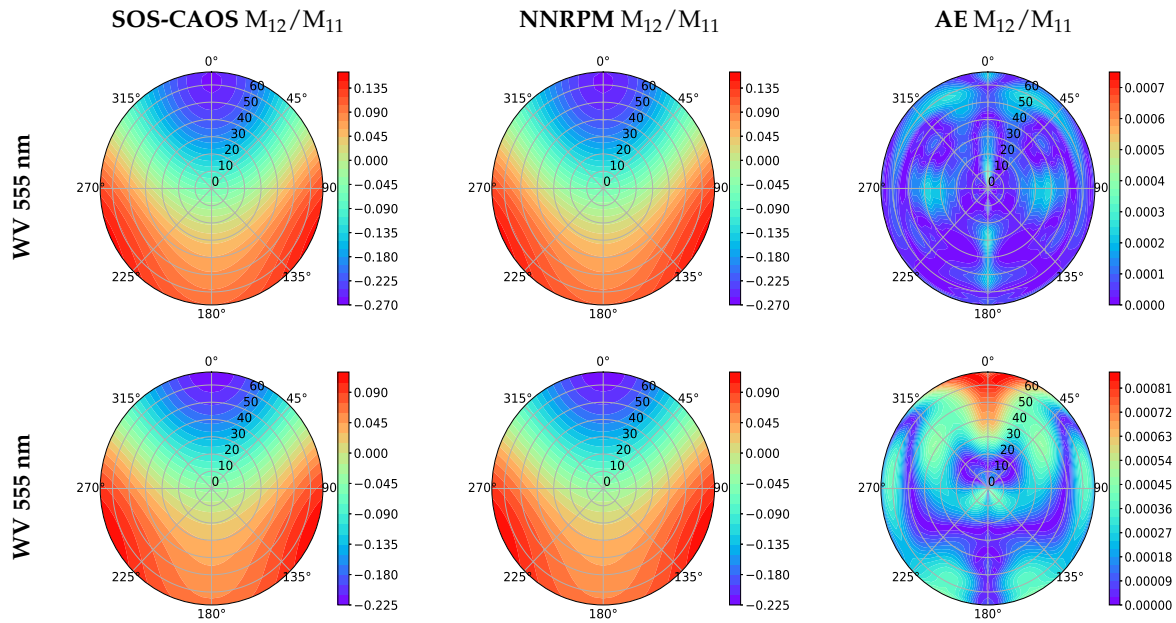
Figure 6. Polar plots of SOS-CAOS, NNRPM and PE for M_{11} at wavelength 555 nm. Input parameters for Top Row: θ_i = 55.91°, Chla = 20.43 mg/m³, $a_{dg}(440)$ = 0.258 m⁻¹, b_{bp} = 0.088 m⁻¹, B_p = 0.016, S_{Bp} = −0.157 nm⁻¹, S_{bp} = 0.258 nm⁻¹, S_{dg} = 0.019 nm⁻¹. Input parameters for Bottom Row: θ_i = 43.02°, Chla = 24.77 mg/m³, $a_{dg}(440)$ = 0.0004 m⁻¹, b_{bp} = 0.098 m⁻¹, B_p = 0.048, S_{Bp} = −0.106 nm⁻¹, S_{bp} = 0.023 nm⁻¹, S_{dg} = 0.014 nm⁻¹.

Figure 7. Polar plots of SOS-CAOS, NNRPM and AE for M_{12}/M_{11} at wavelength 385 nm. Input parameters for Top Row:θ_i = 55.91°, Chla = 20.43 mg/m³, $a_{dg}(440)$ = 7.36 m⁻¹, b_{bp} = 0.097 m⁻¹, B_p = 0.015, S_{Bp} = −0.157 nm⁻¹, S_{bp} = 0.258 nm⁻¹, S_{dg} = 0.019 nm⁻¹. Input parameters for Bottom Row: θ_i = 43.02°, Chla = 24.77 mg/m³, $a_{dg}(440)$ = 0.004 m⁻¹, b_{bp} = 0.099 m⁻¹, B_p = 0.046, S_{Bp} = −0.106 nm⁻¹, S_{bp} = 0.023 nm⁻¹, S_{dg} = 0.014 nm⁻¹.

**Figure 8.** Polar plots of SOS-CAOS, NNRPM and AE for M_{12}/M_{11} at wavelength 555 nm. Input parameters for Top Row: θ_i = 55.91°, Chla = 20.43 mg/m³, $a_{dg}(440)$ = 0.258 m⁻¹, b_{bp} = 0.088 m⁻¹, B_p = 0.016, S_{Bp} = −0.157 nm⁻¹, S_{bp} = 0.258 nm⁻¹, S_{dg} = 0.019 nm⁻¹. Input parameters for Bottom Row: θ_i = 43.02 °, Chla = 24.77 mg/m³, $a_{dg}(440)$ = 0.0004 m⁻¹, b_{bp} = 0.098 m⁻¹, B_p = 0.048, S_{Bp} = −0.106 nm⁻¹, S_{bp} = 0.023 nm⁻¹, S_{dg} = 0.014 nm⁻¹.

In Figure 9, we have shown ECDF versus PE at wavelengths 385 and 555 nm, which shows that ECDF approaches 1 asymptotically as PE increases and becomes very close to 1 when PE is larger than 5%.
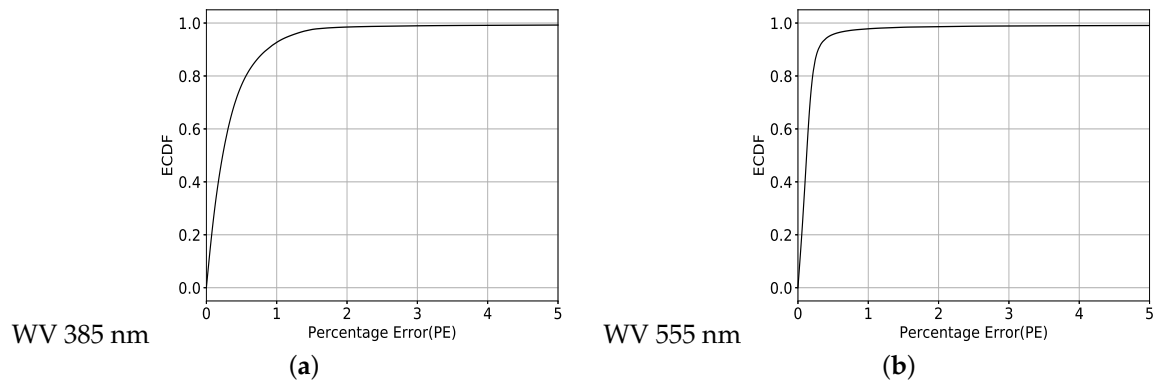
Figure 9. ECDF vs PE for M_{11} at wavelengths (**a**) 385 and (**b**) 555 nm.

In Tables 2–4, the performance of the neural networks corresponding to each element of the Mueller matrix from Equation (4), for every wavelength being studied, has been shown. For evaluating the prediction performance of the degree of linear polarization (DoLP = $\sqrt{Q^2 + U^2}/I$), we tested the AE for the expression $\sqrt{M_{21}^2 + M_{31}^2}/M_{11}$, which is equal to DoLP when the incident light is unpolarized. The results are shown in Table 2. For the first element M_{11}, the NNRPM is able to predict values with percentage error (PE) less than 5% for 99% of the test cases. For the rest of the normalized elements, the NNRPM is able to predict values with absolute error (AE) less than 0.004 for 99% of the test cases. DoLP for unpolarized incident light can be predicted with an absolute error (AE) less than 0.002 for 99% of the test cases.

Table 2. Percentage of cases for element M_{11} with Percentage error (PE) less than 5% and percentage of cases for elements M_{21}/M_{11} and M_{31}/M_{11} with Absolute error (AE) less than 0.004, and Degree Of Linear Polarization.

Wavelength (nm)	M_{11} PE < 5%	M_{21}/M_{11} AE < 0.004	M_{31}/M_{11} AE < 0.004	DoLP AE < 0.002
385	99.64	99.78	99.83	99.23
410	99.25	99.68	99.82	98.90
440	99.39	99.75	99.73	98.97
470	99.24	99.77	99.70	98.98
555	99.29	99.78	99.71	98.79
670	99.29	99.75	99.80	99.02
863.5	99.57	99.93	99.92	99.71
870	99.55	99.94	99.92	99.72

Table 3. Percentage of cases for elements M_{12}/M_{11}, M_{22}/M_{11}, and M_{32}/M_{11} with Absolute error (AE) less than 0.004.

Wavelength (nm)	M_{12}/M_{11} AE < 0.004	M_{22}/M_{11} AE < 0.004	M_{32}/M_{11} AE < 0.004
385	99.67	99.43	99.56
410	99.38	99.64	99.40
440	99.50	99.30	99.37
470	99.26	99.13	99.08
555	98.68	99.54	99.24
670	99.53	99.70	99.667
863.5	99.97	99.68	99.79
870	99.92	99.71	99.72

Table 4. Percentage of cases for elements M_{13}/M_{11}, M_{23}/M_{11}, and M_{33}/M_{11} with Absolute error (AE) of elements less than 0.004.

Wavelength (nm)	M_{13}/M_{11} AE < 0.004	M_{23}/M_{11} AE < 0.004	M_{33}/M_{11} AE < 0.004
385	98.89	99.34	99.42
410	98.83	99.23	99.39
440	98.78	99.05	99.29
470	98.00	98.86	99.17
555	98.20	98.31	99.32
670	98.56	99.52	99.63
863.5	99.95	99.73	99.74
870	99.92	99.69	99.74

The CPU time taken by the SOS-CAOS RT code for the prediction of ocean BRDF is 3 min for a case simulated with the following parameters:

- Order of scattering: 40
- Gaussian quadrature for ocean: 80
- Optical depth of the system (for wavelength 555 nm): 6986.19
- Scattering coefficient of phytoplankton and NAP particles, b_p: 34.468 m^{-1}
- System specifications: 2.8 GHz Intel Core i7 and memory of 16 GB 1600 MHz DDR3

The corresponding time taken by NNRPM is 0.0296 seconds which is mostly stable for an arbitrary case.

4. Discussions

In order to determine the optimum number of training cases required, we experimented with various sets of Halton sequences. We found that accuracy increases as the number of Halton

combinations used in the training increases until it reaches 8000. From Figure 3, we can see that error initially decreases as the training data is increased and reaches a minimum for a certain volume of training data. This result is similar to the error's inverse relationship with number of training instances mentioned in Gallant et al. [57]. Figure 4 shows a linear relationship between the true value represented by SOS-CAOS and the predicted value represented by NNRPM. The value of R-squared being close to 1 indicates clear correlation between the true value (SOS-CAOS) and the predicted value (NNRPM). The slope (m) being close to 1 and bias (y) being close to 0 further confirms the agreement between NNRPM with SOS-CAOS.

The Bidirectional Reflectance Distribution Function (BRDF) is the quantity which geometrically characterizes the reflecting properties of a point on a surface [58]. The angular distribution of the water leaving signals are illustrated through the polar plots in Figures 5 to 8. The SOS-CAOS and NNRPM polar plots provide a pictorial representation of how close the neural network predicted value is to the actual SOS-CAOS value for the specific scenario under consideration. In Figures 5 and 6, the accuracy of the model for the element M_{11} is illustrated by the Percentage error polar plots which has a maximum value around 3%. For test cases with the smaller values of a_{dg}, the values of reflectance will be higher for both wavelengths, and vice versa. In Figures 7 and 8, the accuracy of the model for the element M_{12}/M_{11} is illustrated by the Absolute error polar plots which has a maximum value around 0.0009. We can see that the model is able to predict both positive and negative results equally well.

Figure 9 is the visual representation of how quickly the cumulative distribution function increases to 1. It shows the probability of an unknown test dataset having a percentage error below any chosen threshold. Here we can say that the probability of getting a percentage error of less than 5% across the entire test dataset is close to 1. This further confirms the accuracy of the model on an unseen test dataset.

The simulation time of SOS-CAOS depends on the order of scattering and the number of Gaussian quadratures used for angular integration, which is in turn determined by the required accuracy. Moreover, it also depends upon the total optical depth of the system. Using the parameters mentioned in the results section, we can see that the incorporation of NNRPM would improve the speed of retrieval algorithms by a factor of 6000. For different ocean reflectance cases, the CPU time varies for the SOS-CAOS solution. However the order of magnitude is about the same. Thus the comparison provides a general guideline on the improvement in CPU time.

The future incorporation of this model into the retrieval algorithms will make the retrieval process more efficient, and thus applicable for operational use with global satellite observations. Future work could also examine the necessity of adding more IOPs to these models to simulate the behavior of different water bodies.

5. Conclusions

Ocean polarized reflectances obtained from satellite sensors contains information about the constituents of the upper ocean euphotic zone, such as colored dissolved organic matter (CDOM), sediments, phytoplankton types, and pollutants. Traditional ocean color remote sensing algorithms retrieve the constituent information by first performing atmospheric correction, then deriving IOPs from the resultant remote sensing reflectances. However, atmospheric correction algorithms are still a challenging task for scenes involving coastal waters and absorbing aerosols. In order to overcome this difficulty, joint retrieval algorithms of aerosols and ocean color have been designed to use information in polarized measurements. Joint retrieval algorithms need to solve the radiative transfer equation in atmospheric and ocean coupled system repeatedly, which is resource prohibitive, making them impractical for operational production of satellite data.

In order to resolve this problem, we have built a forward model using machine learning techniques, called Neural Network Reflectance Prediction Model (NNRPM), which can be used to predict ocean bidirectional reflectance, given inherent optical properties of ocean waters. The accuracy of the model

is verified with the test cases generated from radiative transfer code based on the successive order of scattering technique (SOS-CAOS). The NNRPM model is able to predict the reflectance values for the first element with percentage error less than 5% for 99% of the test cases. For the rest of the normalized elements, the NNRPM is able to predict reflectance values with an absolute error less than 0.004 for 99% of the test cases. For unpolarized incident light, the model is able to predict DoLP with an AE less than 0.002 for 99% of test cases. When comparing the average speeds of the NNRPM against the SOS-CAOS model, we see that the NNRPM is able to predict the Ocean BRDF 6000 times faster than SOS-CAOS. The application of this neural network model in inverse algorithms would expedite the retrieval process and make them more efficient for use in global satellite observations. It can also be used in traditional semi-analytical models of retrieving ocean water IOPs, since our bio-optical model is more general than most existing models.

Author Contributions: Conceptualization, L.M., P.-W.Z. and Y.H.; methodology, L.M., P.-W.Z. and M.G.; software, L.M.; validation, L.M.; formal analysis, L.M.; investigation, L.M. and P.-W.Z.; resources, P.-W.Z.; data curation, L.M.; writing—original draft preparation, L.M.; writing—review and editing, L.M., P.-W.Z., M.G., Y.H., B.A.F. and P.J.W.; visualization, L.M. and P.-W.Z.; supervision, P.-W.Z.; project administration, P.-W.Z.; funding acquisition, L.M. and P.-W.Z. All authors have read and agreed to the published version of the manuscript.

Conflicts of Interest: The authors declare no conflict of interest.

References

1. Antoine, D.; Morel, A. A multiple scattering algorithm for atmospheric correction of remotely sensed ocean colour (MERIS instrument): Principle and implementation for atmospheres carrying various aerosols including absorbing ones. *Int. J. Remote Sens.* **1999**, *20*, 1875–1916. [CrossRef]
2. Fukushima, H.; Higurashi, A.; Mitomi, Y.; Nakajima, T.; Noguchi, T.; Tanaka, T.; Toratani, M. Correction of atmospheric effect on ADEOS/OCTS ocean color data: Algorithm description and evaluation of its performance. *J. Oceanogr.* **1998**, *54*, 417–430. [CrossRef]
3. Gordon, H.R.; Wang, M. Retrieval of water-leaving radiance and aerosol optical thickness over the oceans with SeaWiFS: A preliminary algorithm. *Appl. Opt.* **1994**, *33*, 443–452. [CrossRef] [PubMed]
4. Dierssen, H.M. Perspectives on empirical approaches for ocean color remote sensing of chlorophyll in a changing climate. *Proc. Natl. Acad. Sci. USA* **2010**, *107*, 17073–17078. [CrossRef] [PubMed]
5. Hu, C.; Lee, Z.; Franz, B. Chlorophyll aalgorithms for oligotrophic oceans: A novel approach based on three band reflectance difference. *J. Geophys. Res. Oceans* **2012**, *117*, 1–25. [CrossRef]
6. Shanmugam, P.; Ahn, Y.H.; Ryu, J.H.; Sundarabalan, B. An evaluation of inversion models for retrieval of inherent optical properties from ocean color in coastal and open sea waters around Korea. *J. Oceanogr.* **2010**, *66*, 815–830. [CrossRef]
7. Boss, E.; Roesler, C. Over constrained linear matrix inversion with statistical selection. In *Remote Sensing of Inherent Optical Properties: Fundamentals, Tests of Algorithms, and Applications*; Volume 5 of Reports of the International Ocean Colour Coordinating Group; Lee, Z.P., Ed.; IOCCG: Dartmouth, NS, Canada, 2006; pp. 57–62.
8. Garver, S.A.; Siegel, D.A. Inherent optical property inversion of ocean color spectra and its biogeochemical interpretation: 1. Time series from the Sargasso Sea. *J. Geophys. Res. Oceans* **1997**, *102*, 18607–18625. [CrossRef]
9. Maritorena, S.; Siegel, D.A.; Peterson, A.R. Optimization of a semianalytical ocean color model for global-scale applications. *Appl. Opt.* **2002**, *41*, 2705–2714. [CrossRef]
10. Gordon, H.R.; Brown, O.B.; Evans, R.H.; Brown, J.W.; Smith, R.C.; Baker, K.S.; Clark, D.K. A semianalytic radiance model of ocean color. *J. Geophys. Res. Atmos.* **1988**, *93*, 10909–10924. [CrossRef]

11. IOCCG. Remote Sensing of Inherent Optical Properties: Fundamentals, Tests of Algorithms, and Applications. In *Reports of the International Ocean Colour Coordinating Group*; Lee, Z.P., Ed.; IOCCG: Dartmouth, NS, Canada, 2006; Volume 5.

12. Ligi, M.; Kutser, T.; Kallio, K.; Attila, J.; Koponen, S.; Paavel, B.; Soomets, T.; Reinart, A. Testing the performance of empirical remote sensing algorithms in the Baltic Sea waters with modelled and in situ reflectance data. *Oceanologia* **2017**, *59*, 57–68. [CrossRef]

13. Morel, A.; Gentili, B. A simple band ratio technique to quantify the colored dissolved and detrital organic material from ocean color remotely sensed data. *Remote Sens. Environ.* **2009**, *113*, 998–1011. [CrossRef]

14. Franz, B.A.; Werdell, P.J. A generalized framework for modeling of inherent optical properties in ocean remote sensing applications. *Proc. Ocean Opt. Anchorage Alaska* **2010**, *27*, 1–3.

15. Werdell, P.J.; McKinna, L.I.; Boss, E.; Ackleson, S.G.; Craig, S.E.; Gregg, W.W.; Lee, Z.; Maritorena, S.; Roesler, C.S.; Rousseaux, C.S.; et al. An overview of approaches and challenges for retrieving marine inherent optical properties from ocean color remote sensing. *Prog. Oceanogr.* **2018**, *160*, 186–212. [CrossRef] [PubMed]

16. IOCCG. Remote Sensing of Ocean Colour in Coastal, and Other Optically-Complex, Waters. In *Reports of the International Ocean Colour Coordinating Group*; Sathyendranath, S., Ed.; IOCCG: Dartmouth, NS, Canada, 2000; Volume 3.

17. IOCCG. Atmospheric Correction for Remotely-Sensed Ocean-Colour Products. In *Reports of the International Ocean Colour Coordinating Group*; Wang, M., Ed.; IOCCG: Dartmouth, NS, Canada, 2010; Volume 10.

18. Deschamps, P.Y.; Bréon, F.M.; Leroy, M.; Podaire, A.; Bricaud, A.; Buriez, J.C.; Seze, G. The POLDER mission: Instrument characteristics and scientific objectives. *IEEE Trans. Geosci. Remote Sens.* **1994**, *32*, 598–615. [CrossRef]

19. Cairns, B.; Russell, E.E.; Travis, L.D. Research scanning polarimeter: Calibration and ground-based measurements. In Polarization: Measurement, Analysis, and Remote Sensing II. *Int. Soc. Opt. Photonics* **1999**, *3754*, 186–196.

20. Diner, D.J.; Xu, F.; Garay, M.J.; Martonchik, J.V.; Rheingans, B.E.; Geier, S.; Davis, A.; Hancock, B.R.; Jovanovic, V.M.; Bull, M.A.; et al. the Airborne Multiangle SpectroPolarimetric Imager (AirMSPI): A new tool for aerosol and cloud remote sensing. *Atmos. Meas. Tech.* **2013**, *6*, 2007–2025. [CrossRef]

21. Snik, F.; Rietjens, J.H.; Van Harten, G.; Stam, D.M.; Keller, C.U.; Smit, J.M.; Laan, E.C.; Verlaan, A.L.; Ter Horst, R.; Navarro, R.; et al. SPEX: The spectropolarimeter for planetary exploration. Space Telescopes and Instrumentation 2010: Optical, Infrared, and Millimeter Wave. *Int. Soc. Opt. Photonics* **2010**, *7731*. [CrossRef]

22. Martins, J.V.; Fernandez-Borda, R.; McBride, B.; Remer, L.; Barbosa, H.M. The Harp Hype Ran Gular Imaging Polarimeter and the Need for Small Satellite Payloads with High Science Payoff for Earth Science Remote Sensing. In Proceedings of the IGARSS 2018— IEEE International Geoscience and Remote Sensing Symposium, Valencia, Spain, 22–27 July 2018; pp. 6304–6307.

23. Werdell, P.J.; Behrenfeld, M.J.; Bontempi, P.S.; Boss, E.; Cairns, B.; Davis, G.T.; Franz, B.A.; Gliese, U.B.; Gorman, E.T.; Hasekamp, O.; et al. the Plankton, Aerosol, Cloud, ocean Ecosystem mission: Status, science, advances. *Bull. Am. Meteorol. Soc.* **2019**, *100*, 1775–1794. [CrossRef]

24. Chowdhary, J.; Cairns, B.; Mishchenko, M.I.; Hobbs, P.V.; Cota, G.F.; Redemann, J.; Rutledge, K.; Holben, B.N.; Russell, E. Retrieval of aerosol scattering and absorption properties from photopolarimetric observations over the ocean during the CLAMS experiment. *J. Atmos. Sci.* **2005**, *62*, 1093–1117. [CrossRef]

25. Hasekamp, O.P.; Litvinov, P.; Butz, A. Aerosol properties over the ocean from PARASOL multiangle photopolarimetric measurements. *J. Geophys. Res. Atmos.* **2011**, *116*, 2156–2202. [CrossRef]

26. Xu, F.; Dubovik, O.; Zhai, P.W.; Diner, D.J.; Kalashnikova, O.V.; Seidel, F.C.; Litvinov, P.; Bovchaliuk, A.; Garay, M.J.; van Harten, G.; et al. Joint retrieval of aerosol and water-leaving radiance from multispectral, multiangular and polarimetric measurements over ocean. *Atmos. Meas. Tech.* **2016**, *9*, 2877–2907. [CrossRef]

27. Gao, M.; Zhai, P.W.; Franz, B.; Hu, Y.; Knobelspiesse, K.; Werdell, P.J.; Ibrahim, A.; Cairns, B.; Chase, A. Inversion of multi-angular polarimetric measurements over open and coastal ocean waters: A joint retrieval algorithm for aerosol and water leaving radiance properties. *Atmos. Meas. Tech.* **2019**, *12*, 3921–3941. [CrossRef]

28. Fan, C.; Fu, G.; Di Noia, A.; Smit, M.; Rietjens, H.H.J.; Ferrare, A.R.; Burton, S.; Li, Z.; Hasekamp, P.O. Use of a Neural Network-Based Ocean Body Radiative Transfer Model for Aerosol Retrievals from Multi-Angle Polarimetric Measurements. *Remote Sens.* **2019**, *11*, 2877. [CrossRef]

29. Gao, M.; Zhai, P.W.; Franz, B.; Hu, Y.; Knobelspiesse, K.; Werdell, P.J.; Ibrahim, A.; Xu, F.; Cairns, B. Retrieval of aerosol properties and water-leaving reflectance from multi-angular polarimetric measurements over coastal waters. *Opt. Express* **2018**, *26*, 8968–8989. [CrossRef] [PubMed]

30. Kou, L.; Labrie, D.; Chylek, P. Refractive indices of water and ice in the 0.65-to 2.5-μm spectral range. *Appl. Opt.* **1993**, *32*, 3531–3540. [CrossRef] [PubMed]

31. Pope, R.M.; Fry, E.S. Absorption spectrum (380–700 nm) of pure water. II. Integrating cavity measurements. *Appl. Opt.* **1997**, *36*, 8710–8723. [CrossRef]

32. Zhang, X.; Hu, L. Scattering by pure seawater at high salinity. *Opt. Express* **2009**, *17*, 12685–12691. [CrossRef]

33. Morel, A. Optical properties of pure water and pure sea water. *Opt. Asp. Oceanogr.* **1974**, *1*, 1–24.

34. Bricaud, A.; Morel, A.; Babin, M.; Allali, K.; Claustre, H. Variations of light absorption by suspended particles with chlorophyll a concentration in oceanic (case 1) waters: Analysis and implications for bio-optical models. *J. Geophys. Res. Oceans* **1998**, *103*, 31033–31044. [CrossRef]

35. Werdell, P.J.; Franz, B.A.; Bailey, S.W.; Feldman, G.C.; Claustre, H. Generalized ocean color inversion model for retrieving marine inherent optical properties. *Appl. Opt.* **2013**, *52*, 2019–2037. [CrossRef]

36. Werdell, P.J.; McKinna, L.I.W. Sensitivity of Inherent Optical Properties From Ocean Reflectance Inversion Models to Satellite Instrument Wavelength Suites. *Front. Earth Sci.* **2019**, *7*, 54. [CrossRef] [PubMed]

37. Fournier, G.R.; Forand, J.L. Analytic phase function for ocean water. In *Ocean Optics XII*; International Society for Optics and Photonics: Bergen, Norway, 1994; pp. 194–201.

38. Sullivan, J.M.; Twardowski, M.S. Angular shape of the oceanic particulate volume scattering function in the backward direction. *Appl. Opt.* **2009**, *48*, 6811–6819. [CrossRef] [PubMed]

39. Mobley, C.D.; Sundman, L.K. Phase function effects on oceanic light fields. *Appl. Opt.* **2002**, *41*, 1035–1050. [CrossRef] [PubMed]

40. Voss, K.J.; Fry, E.S. Measurement of the Mueller matrix for ocean water. *Appl. Opt.* **1984**, *23*, 4427–4439. [CrossRef]

41. Kokhanovsky, A.A. Parameterization of the Mueller matrix of oceanic waters. *J. Geophys. Res. Oceans* **2003**, *108*, 3175. [CrossRef]

42. Zhai, P.W.; Knobelspiesse, K.; Ibrahim, A.; Franz, B.A. Water-leaving contribution to polarized radiation field over ocean. *Opt. Express* **2017**, *25*, A689–A708. [CrossRef]

43. Zhai, P.W.; Hu, Y.; Trepte, C.R.; Lucker, P.L. A vector radiative transfer model for coupled atmosphere and ocean systems based on successive order of scattering method. *Opt. Express* **2009**, *17*, 2057–2079. [CrossRef]

44. Zhai, P.W.; Yongxiang H.; Chowdhary, J.; Trepte, C.R.; Lucker, P.L.; Josset, D.B. A vector radiative transfer model for coupled atmosphere and ocean systems with a rough interface. *J. Quant. Spectrosc. Radiat. Transf.* **2010**, *111*, 1025–1040. [CrossRef]

45. Lawless, R.; Xie, Y.; Yang, P.; Kattawar, G.W.; Laszlo, I. Polarization and effective Mueller matrix for multiple scattering of light by nonspherical ice crystals. *Opt. Express* **2006**, *14*, 6381–6393. [CrossRef]

46. Kattawar, G.W.; Adams, C.N. Stokes vector calculations of the submarine light field in an atmosphere-ocean with scattering according to a Rayleigh phase matrix: Effect of interface refractive index on radiance and polarization. *Limnol. Oceanogr.* **1989**, *34*, 1453–1472. [CrossRef]

47. MathWorks. *Deep Learning Toolbox*; The MathWorks Inc.: Natick, MA, USA, 2019.

48. Smith, J.A. LAI inversion using a back-propagation neural network trained with a multiple scattering model. *IEEE Trans. Geosci. Remote Sens.* **1993**, *31*, 1102–1106. [CrossRef]

49. Smith, J.A. Multilayer feedforward networks are universal approximators. *Neural Netw.* **1989**, *2*, 359–366.

50. Abuelgasim, A.A.; Gopal, S.; Strahler, A.H. Forward and inverse modelling of canopy directional reflectance using a neural network. *Int. J. Remote Sens.* **1998**, *19*, 453–471. [CrossRef]

51. Gron. A. *Hands-On Machine Learning with Scikit-Learn and TensorFlow: Concepts, Tools, and Techniques to Build Intelligent Systems*, 1st ed.; O'Reilly Media, Inc.: Newton, MA, USA, 2017.

52. Marquardt, D.W. An algorithm for least-squares estimation of nonlinear parameters. *J. Soc. Ind. Appl. Math.* **1963**, *11*, 431–441. [CrossRef]

53. Loyola, R.; Diego, G.; Pedergnana, M.; Gimeno, S.G. Smart sampling and incremental function learning for very large high dimensional data. *Neural Netw.* **2016**, *78*, 75–87. [CrossRef]

54. Halton, J.H. On the efficiency of certain quasi-random sequences of points in evaluating multi-dimensional integrals. *Numer. Math.* **1960**, *2*, 84–90. [CrossRef]

55. Pernot, P.; Savin, A. Probabilistic performance estimators for computational chemistry methods: The empirical cumulative distribution function of absolute errors. *J. Chem. Phys.* **2018**, *148*, 241707. [CrossRef]

56. James, G.; Witten, D.; Hastie, T.; Tibshirani, R. *An Introduction to Statistical Learning: With Applications in R*; Springer Publishing Company: Berlin, Germany, 2014.

57. Gallant, A.R.; White, H. There exists a neural network that does not make avoidable mistakes. In Proceedings of the International Conference on Neural Networks, San Diego, CA, USA, 24–27 July 1988.

58. Nicodemus, F.E.; Richmond, J.C.; Hsia, J.J.; Ginsberg, I.W.; Limperis, T. *Geometrical Considerations and Nomenclature for Reflectance*; NBS Monograph; National Bureau of Standards: Washington, DC, USA, 1992.